Tectonophysics 801 (2021) 228720

Contents lists available at ScienceDirect

Tectonophysics

journal homepage: www.elsevier.com/locate/tecto

The 2014 Juan Fernández microplate earthquake doublet: Evidence for large thrust faulting driven by microplate rotation

Simone Cesca [a,*], Carla Valenzuela Malebrán [a,b], José Ángel López-Comino [b,c,d], Timothy Davis [a,b], Carlos Tassara [e], Onno Oncken [a], Torsten Dahm [a,b]

[a] Helmholtz-Zentrum Potsdam Deutsches GeoForschungsZentrum, Potsdam, Germany
[b] Institute of Earth and Environmental Sciences, University of Potsdam, Potsdam, Germany
[c] Instituto Andaluz de Geofísica, Universidad de Granada, Granada, Spain
[d] Departamento de Física Teórica y del Cosmos, Universidad de Granada, Granada, Spain
[e] Universidad Nacional Arturo Prat, Iquique, Chile

ARTICLE INFO

Keywords:
Seismic doublet
Moment tensor
Rupture directivity
Juan Fernández microplate

ABSTRACT

On October 9, 2014, a Mw 7.1–6.7 seismic doublet occurred at the Juan Fernández microplate, close to the triple junction with Pacific and Nazca plates. The Mw 7.1 earthquake is the largest earthquake ever to have been recorded in the region. Its thrust focal mechanism is also unusual for the region, although the northern part of the microplate is expected to undergo compression. The region is remote and seismological data is limited to a seismic station at ~600 km distance on Easter Island and teleseismic observations for the largest events. We use a combination of advanced seismological techniques to overcome the lack of local data and resolve earthquake source parameters for the doublet and its aftershock sequence, being able to reconstruct the chronology of the sequence and the geometry of affected fault segments. Our results depict a complex seismic sequence characterized by the interplay of thrust and strike-slip earthquakes along different structures, including a second, reversed strike slip-thrust seismic doublet in November 2014. Seismicity occurred within the microplate and only in the late part of the sequence migrated northward, towards the microplate boundary. The first largest doublet, whose rupture kinematic is well explained by stress changes imparted by the first subevent on the second one, may have activated unmapped *E*-W and NE-SW faults or an internal curved pseudofault, attributed to the long-term rotation of the microplate. Few large, thrust earthquakes are observed within the sequence, taking place in the vicinity of mapped compressional ridges. We suggest that compressional stresses in the northern part of the microplate and at its boundary are partially accommodated aseismically. However, the occasional occurrence of large, impulsive thrust earthquakes, with a considerable tsunamigenic potential, poses a relevant hazard for islands in the South Pacific region.

1. Introduction

The Juan Fernandez Microplate (JFMP) is a small oceanic plate located in the Pacific region at the triple junction of the Pacific (PP), Nazca (NP) and Antarctic (AP) plates (Larson et al., 1992; Searle et al., 1993; Bird, 2003). The microplate extends for about 410 × 270 km, located at about 32–35°Lat S and 109–112 Lon W (Bird, 2003) along the super-fast spreading East Pacific Rise. The discovery of the JFMP dates to the early 70s and is attributed to Herron (1972) and Forsyth (1972), who proposed its existence on the basis of the distribution of seismicity and focal mechanisms (Barazangi and Dorman, 1969; Forsyth, 1972; Anderson et al., 1974). The microplate was named after the Spanish explorer and navigator Juan Fernández and the group of islands bearing his name (Craig et al., 1983), despite the fact that they actually lay more than 2000 km to the east. The JFMP is one of the largest microplates along the East Pacific rise and one among those located at a triple junction (Larson et al., 1992). The first mapping of its Eastern and Western ridges along the East Pacific Rise at 31–35° Lat S (Craig et al. 1983) was later complemented by a first geophysical survey (Anderson-Fontana et al., 1986), including mapping of bathymetry and magnetic anomalies. Further surveys (Francheteau et al., 1987; Yelles-Chaouche et al., 1987) helped to reconstruct the divergent JFMP-NP and JFMP-PP

* Corresponding author at: Helmholtz-Zentrum Potsdam Deutsches GeoForschungsZentrum, Section 2.1, 14473 Telegrafenberg, Potsdam, Germany.
E-mail addresses: simone.cesca@gfz-potsdam.de, cesca@gfz-potsdam.de (S. Cesca).

https://doi.org/10.1016/j.tecto.2021.228720
Received 26 August 2020; Received in revised form 21 December 2020; Accepted 26 December 2020
Available online 9 January 2021

plate boundaries (JFMP Eastern and Western Ridges, respectively): The Eastern Ridge experienced crustal accretion over the past 4 Myr, while the northern segment of the Western Ridge contains a large overlapping spreading centre (Larson et al., 1992). Combining local mapping with seismicity and slip vector information, the microplate outline and its Euler vectors could be defined (Anderson-Fontana et al., 1986). Since Euler poles lie on the JFMP or within a few hundred kilometers, a large rotational motion of the microplate has been inferred (Larson et al., 1992). The plate boundary database by Bird (2003) reports for the JFMP a Euler pole at 35.910° Lat N, 70.166° Lon E, with a rotation rate of 22.52°/Ma after Anderson-Fontana et al. (1986) and plate boundary after Larson et al. (1992).

It is estimated that the JFMP formed about 4–6 Ma ago. Similarly to the neighbouring Easter Island Microplate, the JFMP kinematic has been described by a so-called "roller-bearing" model (Larson et al., 1992; Searle et al., 1993; Bird et al., 1998), where the JFMP rotates quasi-rigidly with at least two Euler poles located in the close vicinity of the microplate boundaries and with small internal deformation. According

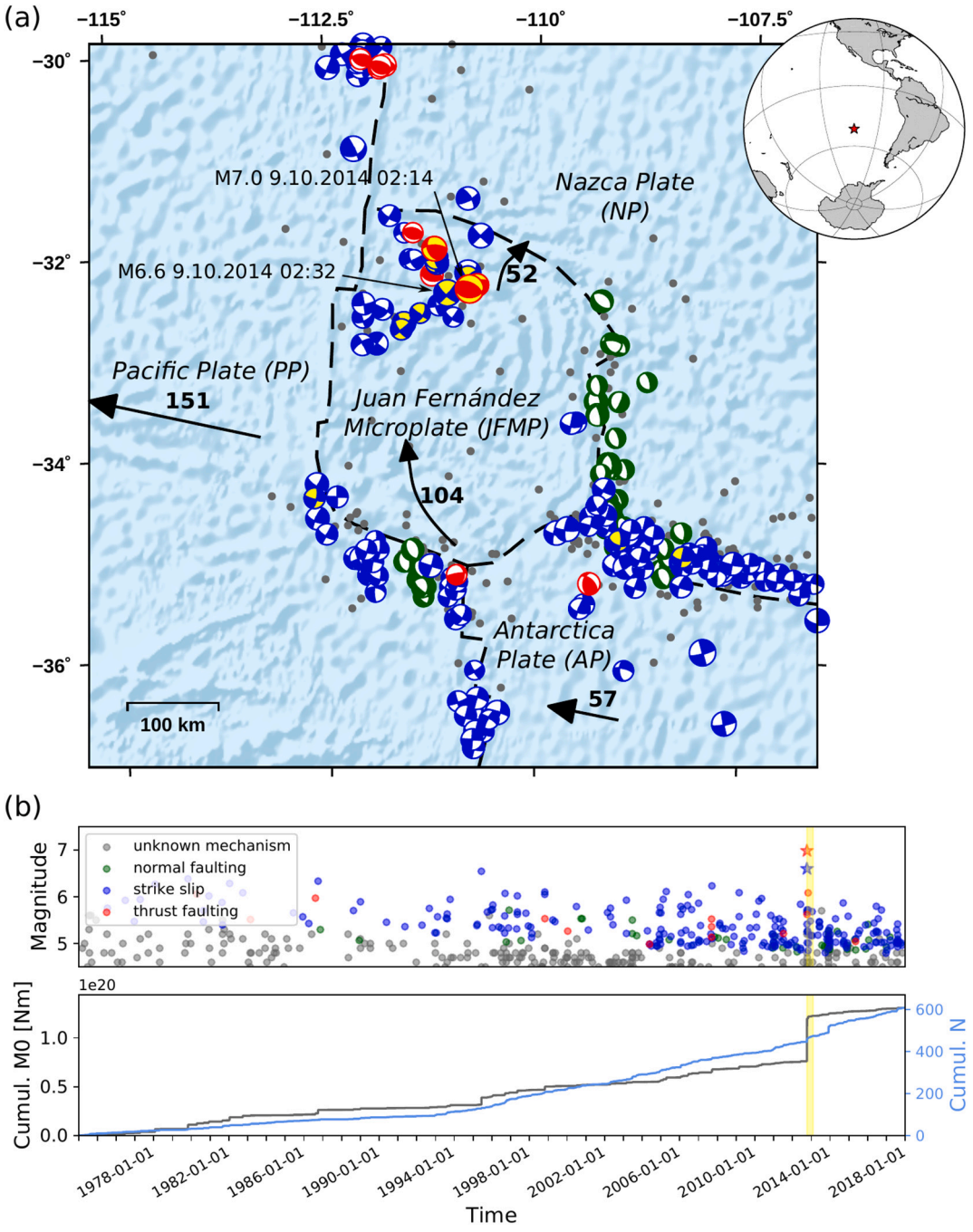

Fig. 1. Seismicity at the Juan Fernández microplate. (a) Spatial distribution of seismicity in the years 2000–2019 (joint catalogs of Global CMT and USGS), showing locations (gray circles) and focal mechanisms, when available (focal sphere coloured according to the legend in (b): normal faulting in green, strike-slip in blue, thrusts in red). Events with focal mechanisms occurring within 120 days since the doublet are identified by yellow pressure quadrants). The location and mechanisms of the doublet are highlighted by black arrows. Dashed black lines denote plate boundaries and dashed arrows the average relative plate velocity with respect to the Nazca plate, bold numbers indicating velocity values in mm/a (after Bird, 2003). (b) Timeline of seismicity showing magnitude, cumulative scalar moment and cumulative number of events as a function of time (joint Global CMT and USGS catalog). (For interpretation of the references to colour in this figure legend, the reader is referred to the web version of this article.)

to the roller-bearing model (Schouten et al., 1988), shear motion at microplate boundaries can apply a torque, which acts as driver for the microplate rotation. In such a model, the microplate is instantaneously in contact with bounding plates at two points, where the plate motions are tangential to the microplate outline. The tectonic history of the JFMP has undergone different phases, which have been reconstructed by Bird et al. (1998), experiencing an overall clockwise rotation. The microplate rotation was originally driven by a faster shear motion imposed by the PP and NP. However, the progressive decoupling from the PP and coupling to the AP resulted in the continuation of the clockwise rotation, but now driven by the NP and AP (Larson et al., 1992) and at a slower pace of ~22.5°/Ma (Anderson-Fontana et al., 1986; Bird, 2003). Eastern and western boundaries of the JFMP are well delineated (Larson et al., 1992) and marked by strike-slip earthquakes (Global CMT). The East Ridge is propagating northwards and the West Ridge southwards, consistent with the prediction of the roller bearing model. The rotation is accompanied by formation of curved pseudofaults both inside and outside the JFMP; inner and outer pseudofaults have been mapped at the Western and Eastern Ridges, progressively growing and bending with the rotation of the microplate (Larson et al., 1992; Searle et al., 1993). Psuedofaults refer here to the traces of propagating ridge tips (Hey, 1977; Searle et al., 1993). East and West ridges appear segmented, with single segments varying 15–135 km in length (Searle et al., 1993). On the contrary, the northern boundary is diffuse and predicted to be under compressional stress (Anderson-Fontana et al., 1986; Naar et al., 1991). However, no thrust earthquakes are known in the region prior to 2014. As for the East Pacific Rise section, which extends to the north of the JFMP until it meets the Easter Island Microplate, and is also relevant to our study, it has been suggested that it undergoes a cyclic contrary propagation and failure of two overlapping spreading centres, without the formation of an additional microplate (Hey et al., 1995; Martinez et al., 1997).

The first dedicated seismicity analysis (Sykes, 1967; Forsyth, 1972; Anderson et al., 1974; Anderson-Fontana et al., 1986), available for a few events in the study region, identified only strike-slip focal mechanisms. Nowadays, broader information is available for the following decades thanks to global seismic catalogs e.g. by Global CMT (Dziewonski et al., 1981; Ekström et al., 2012) and USGS (https://earthquake.usgs.gov/, last accessed 1.7.2020), which provide hundreds of moment tensors at the JFMP boundaries. Looking at the distribution of hypocenters and focal mechanisms until fall 2014, the seismicity at the plate boundary is found to be discontinuous and to reflect the complex motion and the segmented boundaries of the microplate (Fig. 1); until 2014 the peak magnitude was Mw 6.5 (June 10, 1997). The JFMP rotation and shearing to neighbouring plates have been seismically accommodated by a majority of left lateral strike-slip earthquakes along transform segments of the microplate margins. NS oriented normal faulting dominates along the Eastern Ridge and at the southernmost part of the Western Ridge, next to the JFMP-PP-AP triple junction. Very few thrust mechanisms are observed, even at the northern JFMP boundary, which should experience local compression. Three low seismicity regions are found at the Northern (JFMP-NP) and Southern (JFMP-AP) microplate boundaries, and at the central segment of the Western Ridge (JFMP-PP).

On October 9, 2014, a Mw 7.1–6.7 seismic doublet (Mw 6.9–6.6 according to Global CMT) occurred close to the PP-NP-JFMP triple junction, but apparently within the microplate (Fig. 1). The two events in the doublet, occurring less than 20 min apart, are the largest ever recorded at the JFMP and the stronger one exceeds any previous earthquake in the region by half a magnitude. Also peculiar was the focal mechanism of the largest subevent, characterized, according to Global CMT, as a pure thrust mechanism. Here, we study in detail the rupture process of the doublet and its seismic sequence, by means of moment tensor inversion, waveform similarity, rupture directivity modelling, rupture geometry mapping and Coulomb stress analysis, to investigate their role in the framework of the JFPM rotational kinematics.

2. The 2014 seismic doublet at the Juan Fernández microplate

The seismic sequence started on October 9, 2014, at 2:14:42 UTC, with a Mw 7.1 earthquake striking at Lat 32.34° S, Lon 110.81° W (centroid location by Global CMT) in the Northernmost part of the JFMP (from now on referred as the first subevent). The Global CMT catalog reports a thrust mechanism oriented roughly ESE-WNW at a fixed shallow depth of 12 km and an unusually short (11.0 s) difference among hypocenter and centroid times, suggesting an impulsive earthquake with short rupture duration. Even accounting for the remoteness of the study region and the poor earthquake detectability (minimum magnitudes reported by Global CMT are above Mw ~5.5 before 1990, and above Mw ~ 5.0 in the period 1990–2006), thrust earthquakes are extremely rare in the region, and there are no reported cases of Mw 6+ with such mechanism in the region prior to 2014. Only 18 min later, at 2:32:14 UTC, a second earthquake occurred (hereon referred as the second subevent), with magnitude Mw 6.7; Global CMT reports a depth of 18 km, strike-slip mechanism and a centroid located about 25 km WSW of the first shock. The differential centroid-hypocenter time of 9.3 s is only slightly shorter than for the first subevent, besides from a significantly weaker magnitude. Unexpectedly for seismicity close to the mid oceanic ridge, the doublet generated a moderate tsunami: tide gages measured peak tide amplitudes of 47 cm at Easter Island, Chile, ~10 cm at Santa Cruz, Galapagos, Ecuador and at San Felix and Bahia Mansa, Chile, and <5 cm at Juan Fernandez, Chile (www.tsunami.gov, last visited 1.7.2020).

The doublet presents two uneven focal mechanisms, with a first, larger thrust event and a second strike-slip event: while seismic doublets with different focal mechanisms have been observed in the past (e.g. Ghods et al., 2015; Liu and Zahradník, 2020), they remain relatively rare, especially for doublets of such large magnitude. Earthquake doublets and multiplets have been observed globally (Kagan and Jackson, 1999) and they have been studied to map stress heterogeneities at plate boundaries, and understand the behaviour of complex fault systems and earthquake triggering (e.g. Lay and Kanamori, 1980; Astiz and Kanamori, 1984; Lay et al., 2013; Zahradník et al., 2017; Danré et al., 2019; Niazpour et al., 2020). Waveforms of the two earthquakes recorded at the closest broadband station on Easter Island (seismic station Rapa Nui, RPN, of the Global Seismograph Network - IRIS/IDA (GSN) network, Scripps Institution Of Oceanography, 1986) are shown in Fig. 2. The difference among seismic signals, as well as different amplitude ratios among vertical (LHZ) and horizontal (LH1,LH2) components, are clearly visible both in the high and low frequency bands and are illustrative of the different focal mechanisms of the two subevents, despite their close locations.

The earthquake doublet was followed by a seismic sequence, with 13 additional events above Mw 4.4 reported (joint USGS and Global CMT catalogs) in the following week. Global CMT reports focal mechanisms for 9 of these aftershocks: surprisingly, all these solutions except one, propose strike-slip mechanisms well compatible with the second, weaker subevent, against a single thrust mechanism similar to the first, larger subevent. After a quiescence period of about 15 days, seismicity took over again North and Northwest of the doublet, with three earthquakes above magnitude Mw 4.9. In particular, a new doublet was observed on November 1, 2014, with a reversed sorting: first a strike-slip subevent (Mw 5.7, at 10:05:47 UTC), followed by a thrust subevent (Mw 6.1, at 11:00:00 UTC), and focal mechanisms according to Global GMT moment tensor solutions.

3. Moment tensor inversion and rupture directivity

Here, we extend the source analysis of the seismic doublet by means of moment tensor (MT) inversion and rupture directivity analysis. Seismic sources of the aftershocks and the following seismic sequence, including the later doublet in November, are studied by a combination of MT inversion and waveform similarity analysis. Our aim is to confirm

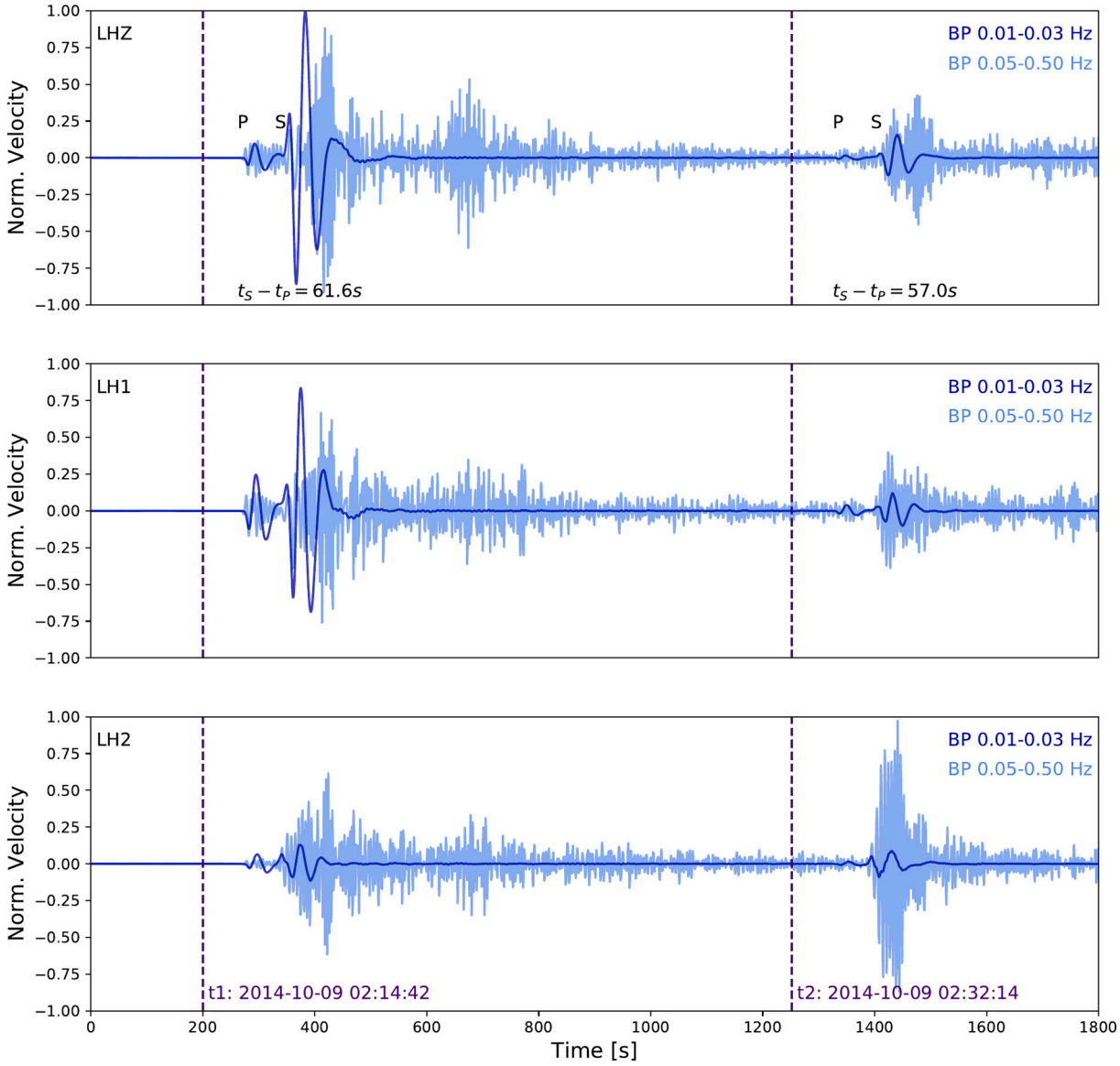

Fig. 2. Example of the earthquake doublet seismic waveforms in two different frequency bands (0.01–0.03 Hz dark blue, 0.05–0.50 Hz light blue), recorded at the station II.RPN.00, Easter Island, Chile, which is the closest seismic station, located at ~600 km epicentral distance. Vertical dashed lines denote the origin time (t1, t2) of the two events of the doublet. P and S picks and differential t_S-t_P times at RPN for the two subevents are reported in the top panel. The difference in the focal mechanisms is responsible for the different ratio among maximal amplitude in different components. (For interpretation of the references to colour in this figure legend, the reader is referred to the web version of this article.)

and extend previous seismological results to reconstruct the geometry of activated fault(s) and track the temporal evolution of seismicity. This analysis will also help the discussion of anomalous earthquake source parameters (e.g. unusual rupture duration) and aftershock productivity (e.g. rate of thrust vs strike-slip aftershocks).

Moment tensor inversion has been first performed for the seismic doublet and for the largest earthquakes in the sequence using the Grond software (Heimann et al., 2018), based on seismic data at regional to teleseismic distances (Fig. S1). For the first subevent we simultaneously fit the following observations: (1) full waveform displacements on vertical, radial and transversal components (360 s time windows, bandpass 0.01–0.03 Hz) and corresponding amplitude spectra at closest stations (below 3000 km) II.RPN.10 and IU.PTCN.01, (2) P wave waveforms on the vertical component (60 s time windows, bandpass 0.02–0.05 Hz) and S wave waveforms on the transversal component (90 s time windows, bandpass 0.02–0.05 Hz) on the vertical components (both fitting amplitude spectra and cross-correlation in the time domain) for open broadband stations at a distance of 3000–5000 km. For the second subevent we used the same setup, except that we avoid using P waveforms at a far distance, as they overlap with the energetic signal of the first subevent. For the remaining studied events (i.e. those with Mw 5.5+) we follow a similar approach as for the first subevent, but use a slightly higher frequency ba2d (0.02–0.06 Hz for all observations), given the lower earthquake magnitudes. The selection of such a magnitude-dependent frequency band is not unusual (e.g. Ekström et al., 2012) and driven by our wish to fit low frequency waveforms, which are less sensitive to the modelling of wave propagation in a simplified 1D model, while showing good signal-to-noise ratios. Synthetic seismograms and spectra are built for all inversions using a model with an oceanic crust (6.5 km thick, see Fig. S2) above an AK135 global mantle model, given that the majority of ray paths to seismic stations at regional distances or far distance to the Pacific coast of South America, Central America, Antarctica and Pacific islands mostly cross oceanic crust regions. We assume no isotropic component and invert for a deviatoric

moment tensor. Note that the software Grond provides source parameter estimates with uncertainties, estimated by a bootstrap approach on the available data (Heimann et al., 2018). The main results of the moment tensor inversion are reported in Fig. 3 (seismic doublet), Fig. 4 and Table 1 (whole sequence). Full data fits for the doublet are shown in the supplementary material (Figs. S3-S7).

Results of the doublet are in general agreement with those of Global CMT: we obtain similar thrust and strike-slip mechanisms for the two subevents (fault plane angles are reported in Table 1), but estimate slightly larger magnitudes (Mw 7.1 and 6.7 for the two subevents, respectively) and slightly shallower depths (5.6 ± 3.9 km and 12.3 ± 4.5 km for the two subevents, respectively). Non-double-couple (non-DC) components are scattered and poorly resolved, providing no clear evidence for any reliable deviation from a pure DC model. We also invert for the rupture duration and obtain values of ~10 and 14 s, respectively. The short duration estimated for the first subevent is in very good agreement with the source time function by the SCARDEC database (Vallée and Douet, 2016), which shows that most moment is released within the first 10 s, and confirms the unusual short duration of the first subevent, which is here found to be even shorter than for the second one, in spite of having a larger magnitude (Mw 7.1 vs 6.7). Moment tensor solutions, source parameters and example of waveform fits are shown in Fig. 3.

Moment tensors are resolved for 5 more events in the seismic sequence with magnitudes in the range Mw 5.7–6.1, including three aftershocks in the first 30 h following the large doublet and the two events composing the later doublet on November 1, 2014: these include three strike-slip earthquakes, one oblique mechanism and one pure thrust. The November doublet is composed of a strike-slip mechanism followed (interevent time of less than 1 h) by a thrust event. All centroids are resolved at shallow depths, with strike-slip events consistently located slightly deeper (10–12 km) than thrust earthquakes (4–6 km), including the results of the first doublet. Results are in general agreement with those by Global CMT, except for one event (October 10, 2014, 4:07), where we resolve an oblique mechanism, apparently in between the strike-slip and thrust mechanisms of the October doublet, and Global CMT predicts a pure thrust faulting in agreement with subevent 1. Moment tensor solutions for weaker events are difficult to resolve due to their lower magnitude and the remote epicentral region. The closest stations (RPN and PTCN) are located at ~600 and ~ 2000 km from the doublet, and the next ones at more than 3000 km. We therefore follow a different approach to investigate the focal mechanisms of weaker events. Since all observations are at far distance of hundreds to thousands kilometers and since the seismicity occurs within a relatively compact region, a high waveform similarity can be used to detect events with a similar mechanism. The analysis, illustrated in Fig. 4, has been performed on selected stations/components, chosen to have a low seismic noise contamination and where the waveforms of the two subevents of the doublet show significant differences, and thus it is easiest to differentiate among the two potential focal mechanisms. We performed a waveform cross-correlation among signals of weaker events and reference ones of the two subevents, allowing for time shift to account for slightly different ray paths and timing uncertainties. We finally identified similar waveforms, when the cross-correlation exceeded a threshold of 0.7; this value was chosen to ensure a high waveform similarity, while allowing for the classification of a large number of weak events. At the two closest stations, velocity signals recorded on the BH2 component of station RPN are very different for the strike-slip subevent 1 and the thrust subevent 2, and those on the BHZ component of station PTCN are almost anticorrelated. At a larger distance, BHZ traces at station RAR show a characteristic ringing signal for the strike-slip subevent, which is not present for the thrust subevent (note that similar ringing signals are indeed observed for both subevents, but for different azimuths, suggesting a kind of guided wave traveling over large distances, which is generated more efficiently for certain combinations of source geometries and azimuths). Comparing waveforms of the following events, we can easily classify most of the sources of the seismic sequence, confirming our moment tensor solutions and most of Global CMT ones. The only anomaly, again, is the oblique mechanism aftershock of October 10, where we now infer a predominant strike-slip component. Based on the joint interpretation of our MT solutions, Global CMT ones and the waveform similarity analysis we infer the focal mechanisms for 12 events in the sequence, including the original doublet: only two events present a pure thrust mechanism (subevent 1 of the October doublet and subevent 2 of the November doublet), while all others show similar mechanism and/or waveform as the strike-slip subevent 2. For a few more events, we cannot infer any information on the mechanisms: these events are either occurring shortly after the main doublet or have a weaker magnitude, so that in both cases their signal is noisy and/or overlapped with other strong signals.

A full finite source inversion can hardly be performed here, given the lack of local stations. Instead, we try to resolve the main rupture directivity features, which can help to reconstruct the geometry of the doublet. Two approaches are tested, based on the analysis of apparent rupture durations and one comparing the hypocentral and centroid locations, respectively. The first approach (Cesca et al., 2011; López-Comino et al., 2012, 2016) is based on the analysis of apparent rupture durations at different azimuths using P waveforms recorded at regional to teleseismic distances (Fig. 5). Although the network is asymmetric, with many stations located East of the epicentral region along the coast of South America, the availability of some stations on the Pacific islands, Antarctica and Central America helps to reduce the azimuthal gap. Unfortunately, this approach can only be used for the first subevent, because the P signals of the second subevent are in most cases overlapping with stronger S and coda signals from the first one. We calculated the normalized energy signals (square amplitude derived from the displacement) following the P-wave onset at different stations (Fig. 5a). The selected seismic stations show a good-quality recording in the P-phase with a maximum epicentral distance of 4961 km; note the closest station (RPN) is excluded from this analysis because its epicentral distance is significantly smaller than for all other stations and we prefer to use a homogeneous dataset. Despite the azimuthal gaps of 71° and 88° to the N and SW respectively, an azimuthal pattern is clearly observed in the raw waveforms and P-wave displacements, which can be identified by the delays of peak squared displacement of the P-phase (D^2_{Pmax}). The largest delays of D^2_{Pmax}, corresponding to the largest apparent durations, are found for stations located East and West of the epicenter, while the shortest delays (and apparent durations) are found towards the South. These delays are measured in the range from 5.0 to 9.0 s; they represent the apparent delay among nucleation and centroid times for the first subevents and are used to discuss and quantify the rupture directivity. Assuming a line source (Haskell, 1964), we consider pure unilateral, asymmetric bilateral and pure bilateral rupture models to find the best fitting with this observed data (Fig. 5c). Inversion yields similar L1 misfit (~0.4 s) for both unilateral and bilateral rupture models. However, the resulting rupture directivity towards NNE obtained by the unilateral rupture model appears incompatible with the two potential fault plane strikes identified in the previous MT analysis (Fig. 5b). A NNE rupture directivity could still be possible along the low dip plane, assuming a downdip propagation. Such type of rupture directivity has been observed for subduction earthquakes (e.g. Tilmann et al., 2016), but rarely in other tectonic contexts. Furthermore, considering the thin seismogenic volume at the JFMP, a downdip propagation would be constrained in size. This seems incompatible with the magnitude, duration and rupture length of this earthquake. Conversely, for a pure bilateral rupture model we find an azimuth of 254 ± 10° (WSW - ENE), which is consistent with the fault plane strike of 266° (Table 1). In addition, this bilateral rupture model is defined by the maximum of two opposite unilateral Haskell sources yielding a centroid-origin time delay of 4.7 s (minimum value of the theoretical prediction). The total rupture duration is thus estimated as twice this value (9.4 s), because we consider the delay of D_{Pmax} as representing half of the

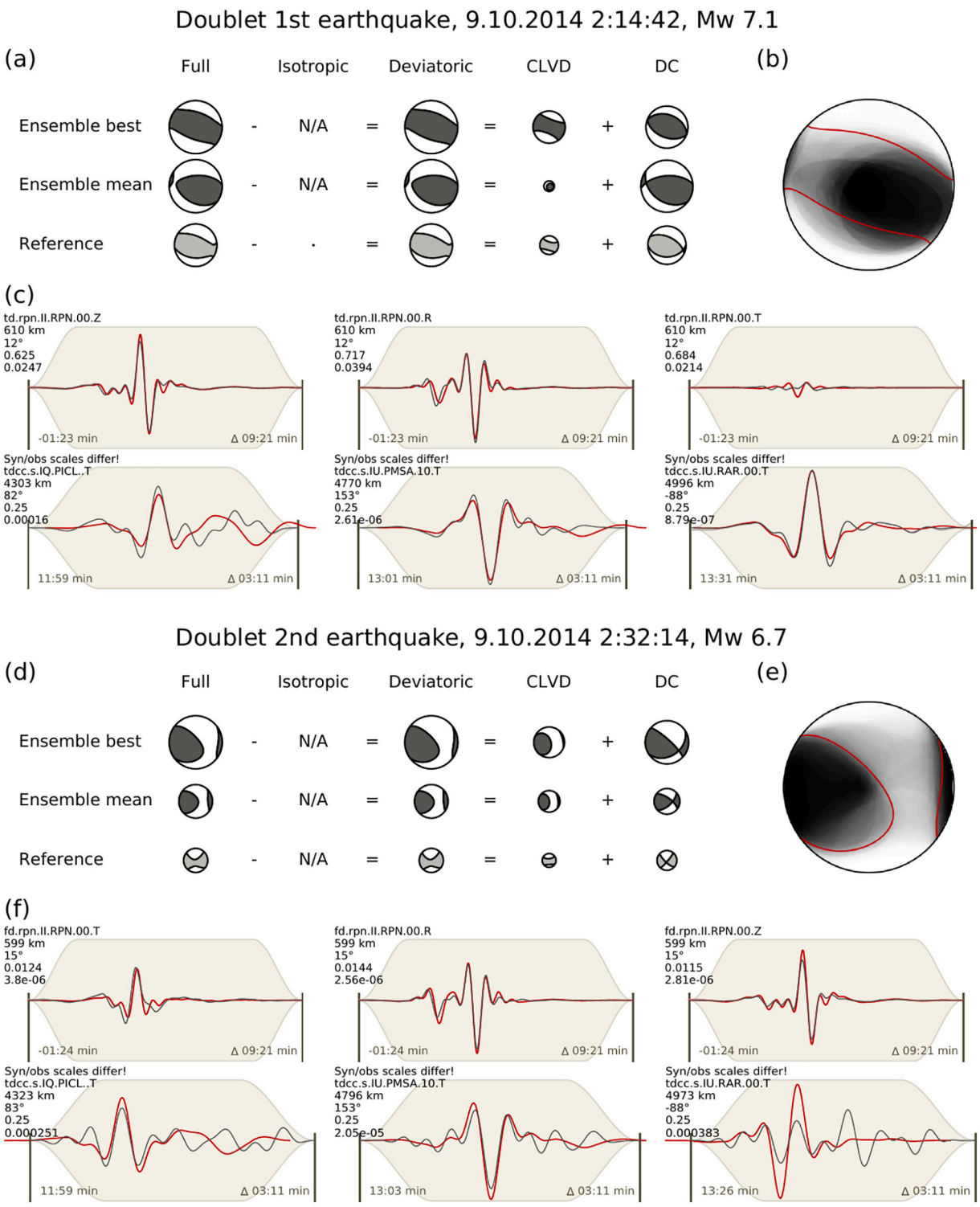

Fig. 3. Summary of moment tensor (MT) inversion results for the October 2014 earthquake doublet (first event plots a-c, second event plots d-f). (a, d) Comparison of MT resolved in this study (black focal sphere), including best and mean (derived from the ensemble of MT solutions obtained by bootstrapping over seismic data) MT solution and the reference Global CMT solution (gray focal sphere); deviatoric MTs are decomposed into isotropic (here forced to zero) and deviatoric MT, and the latter into double couple (DC) and compensated linear vector dipole (CLVD); focal sphere sizes are proportional to scalar moments. (b, e) Fuzzy MT representation, obtained by overlapping semitransparent Mts, obtained for different bootstrap chains (i.e. considering 100 different data configurations), with the best solution marked by thick red lines. (c, f) Example of fits among data (black) and synthetic (red) seismograms for selected stations (data are reported in each plot); the top raw refers to three component of the closest station (IU.RPN.00, Rapa Nui, Easter Island, Chile, at ~600 km distance) and the fit is performed in the time domain for the full waveform, while the lower raw refers to selected far distance (> 4000 km) stations and the fit is performed by cross-correlation of S waves. (For interpretation of the references to colour in this figure legend, the reader is referred to the web version of this article.)

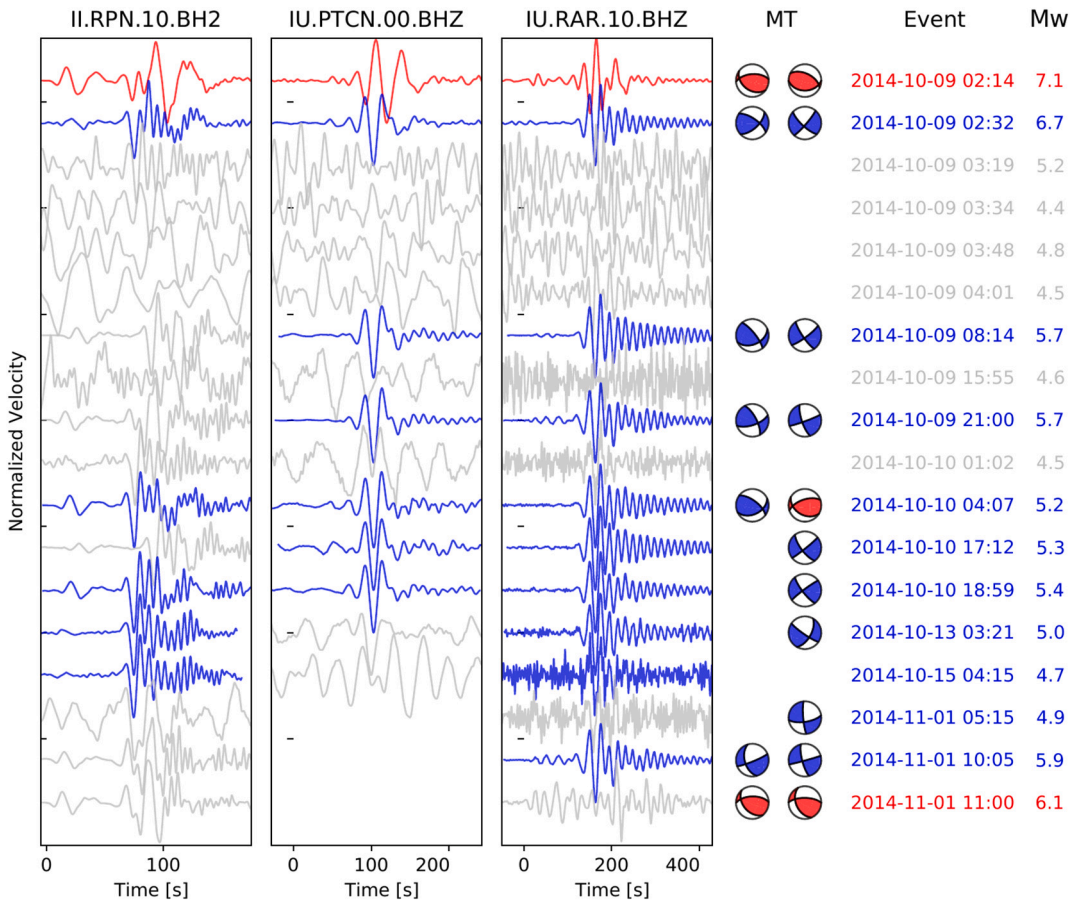

Fig. 4. Summary of waveform comparison and moment tensors (moment tensor inversion out of this study, left, are compared to Global CMT solutions, right) for 18 earthquakes. Normalized waveforms (velocities) are plotted for three selected traces (II.RPN.10.BH2, IU.PTCN.00.BHZ, IU.RAR.10.BHZ); we apply a bandpass filter of 0.02–0.05 Hz (station RPN) and 0.02–0.04 Hz (stations PTCN and RAR). The figure highlights the difference among the waveform of the first subevent (red traces) and the second subevent (blue traces), corresponding with MT similar to first thrust event of the doublet (red focal sphere) or to the second strike-slip event of the doublet (blue focal sphere) focal mechanism. For each of the three traces, waveforms of 18 earthquakes are plotted in red/blue when their waveforms show a high similarity to one of the doublet subevents (cross-correlation coefficient > 0.7), or in gray when the similarity is lower. Labels of each event, reporting data and time, as well as moment magnitude, are plotted in red (thrust), blue (strike-slip) or gray (unknown mechanism), based on the similarity of focal mechanisms and/or waveforms. (For interpretation of the references to colour in this figure legend, the reader is referred to the web version of this article.)

Table 1
Summary of moment tensor inversion result for 7 earthquakes, reporting origin time (date, time), centroid depth, moment magnitude, strike, dip and rake for one plane, compensated linear vector dipole (%), rupture duration and rupture type ('TF' for predominantly thrust faulting, 'SS' for predominantly strike-slip mechanisms). We report here mean values based on the bootstrap analysis performed by Grond (Heimann et al., 2018).

Date	Time	Depth [km]	Mw	Strike [°]	Dip [°]	Rake [°]	CLVD [%]	Duration[s]	Type
9.10.2014	02:14:42	5.6	7.06	266	58	66	4	10.2	TF
9.10.2014	02:32:14	12.3	6.69	48	62	26	41	14.2	SS
9.10.2014	08:14:29	10.8	5.71	66	44	20	-16	4.4	SS
9.10.2014	21:00:02	9.9	5.66	71	66	22	21	4.6	SS
10.10.2014	04:07:57	11.7	5.18	65	43	36	−40	5.1	SS
1.11.2014	10:05:47	10.1	5.90	68	83	−39	−42	5.9	SS
1.11.2014	10:59:58	3.6	6.08	269	59	58	−53	4.1	TF

rupture duration. The resolved rupture duration of ~9 s is in good agreement with the estimation of ~10 s by both our own moment tensor inversion and the SCARDEC database (Vallée and Douet, 2016).

The second approach has been proposed by Zahradnik et al. (2008), in the so-called H—C method, and it is based on the relative hypocentral-centroid location. A significant spatial offset among hypocenter and centroid implies a substantial rupture directivity and the relative location can be used, in favourable conditions, to reconstruct the fault orientation. Here we recollect hypocentral and centroid locations through the International Seismological Centre (ISC) bulletin (International Seismological Centre, 2020) and discuss the relative offset of the most robust locations, i.e. the prime hypocentral location by ISC, and the centroid location by Global CMT. Lateral uncertainties are reported by the ISC bulletin for the prime hypocentral location as ~5 and ~ 7 km for the two subevents. No location uncertainties are reported for the GCMT location. However, Smith and Ekström (1996) reported that relative centroid CMT – hypocentral ISC location uncertainties may be in the order of 25 km and encourage the interpretation of relative location information to derive finite source information (e.g. length, directivity) only for large events (Mw ~ 6.5 and larger) and for relative locations larger than 25 km. The case of the 2014 JFMP doublet is described in Fig. 6. For subevent 1, we do not observe a large spatial offset among

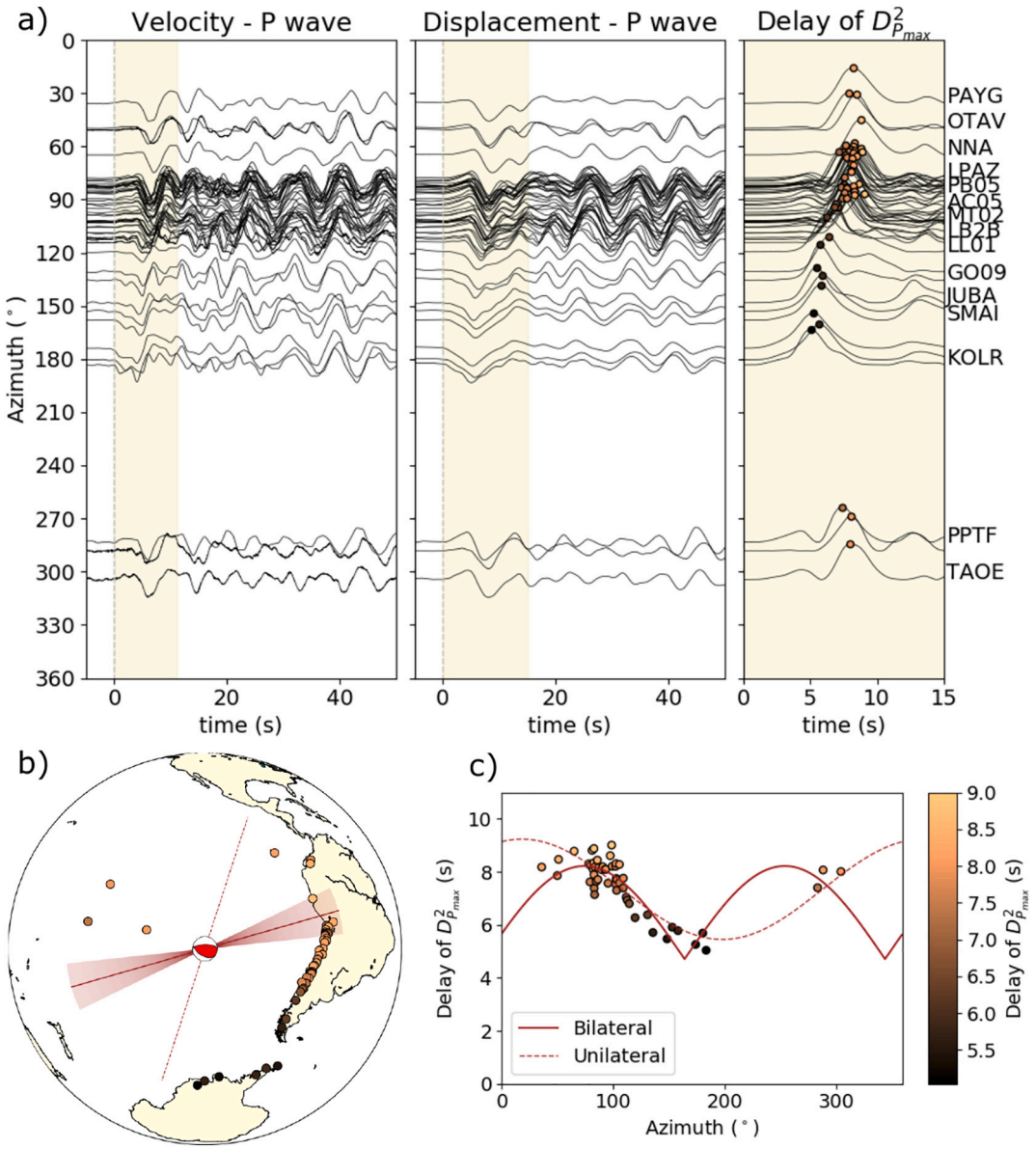

Fig. 5. Directivity analysis for the first subevent of the October 2014 earthquake doublet. a) Raw velocity (left), displacement (middle) and normalized energy signals (right) following the P arrival for the vertical component sorted by azimuth (see station labels). Delays of peak energy of first P phase (D^2_{Pmax}, circles) are plotted in the right panel for each station (colorbar in c). Yellow bands indicate the P-wave window. b) Map of seismic stations used (circles) showing the delay of D^2_{Pmax} (colorbar in c). Focal mechanism, predicted rupture directivities for a unilateral (dashed line) and a bilateral rupture model (solid line) with their uncertainties (brown area) are also shown. c) Delays of D^2_{Pmax} (circles) along with the synthetic predictions for the asymmetric bilateral rupture model (solid line). The direction of unilateral rupture (dashed line) is incompatible with the focal mechanism. (For interpretation of the references to colour in this figure legend, the reader is referred to the web version of this article.)

prime hypocentral location and centroid location, and other locations are quite scattered. In these conditions, the H—C method does not allow a clear discrimination among true and auxiliary fault planes. This may be due to the bilateral rupture directivity, that we proposed based on the first approach, which would explain the relatively small offset among hypocentral and centroid locations. For subevent 2, all proposed hypocentral locations, including the prime location by ISC, lay NE of the centroid location. This suggests a predominantly unilateral rupture from NE to SW, thus clearly favouring the NE-SW fault plane. Both conditions posed by Smith and Ekström (1996) for a safe interpretation of the analysis of relative hyopocentral-centroid locations are fulfilled for subevent 2, what supports our modelling and interpretation.

Joining the different analyses we are able to reconstruct the geometry of the doublet and the evolution of the rupture processes, first bilaterally on an EW oriented thrust segment and then extending the rupture at its Western edge, with a unilateral rupture towards SW, with a strike-slip mechanism.

4. Coulomb stress transfer and earthquake triggering

We model the stresses due to the sub-events using constant slip elastic dislocations in a half-space (King et al., 1994; Nikkhoo and Walter, 2015). Values of the fault patch size, slip and direction are found in Tables 1 and 2 (note rake is defined as the angle away from a pure thrust mechanism, in clock-wise direction when looking down onto the fault). Coulomb stress changes are calculated on planes with a predefined orientation and slip direction.

We now look at static stress changes in the area surrounding the observed events. Firstly, we look at how stress changed on the future fault plane of subevent 2 from the inverted slip of the first subevent

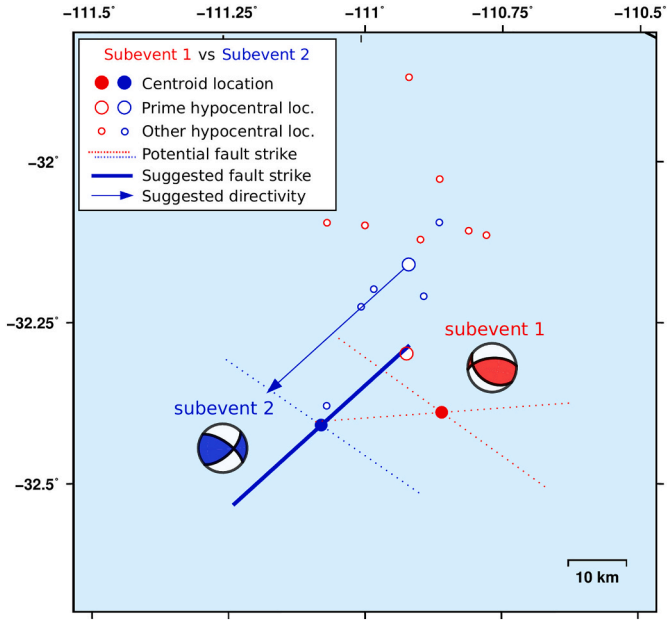

Fig. 6. Summary of hypocenter and centroid locations for the earthquake doublet (subevent 1 in red, subevent 2 in blue). Focal spheres denote DC mechanisms for our moment tensors solutions (Fig. 3). Solid circles are centroid location according to Global CMT, empty circles hypocentral location reported by ISC (large circles denote prime ISC locations). Hypocentral locations for the first subevent are rather scattered and the prime location is close to the centroid one, denoting a bilateral rupture with unclear rupture plane (dotted lines mark the potential fault plane strikes). For the second subevent, a clear NE offset among hypocentral locations (including the prime location) and the centroid location suggests a SW unilateral rupture (blue arrow), in agreement with the NE-SW fault plane (thick solid line, fault plane) and not with the other one (dotted line, auxiliary plane). (For interpretation of the references to colour in this figure legend, the reader is referred to the web version of this article.)

(Fig. 7a). We find that the central and southwestern patch of the second subevent's fault plane is stressed such that left-lateral slip is promoted, while parts of the fault plane north of the first sub-event have a reduced tendency to slide. Overall, this is consistent with the Southward propagation of the rupture front derived by the kinematic modelling, with the rupture nucleating close to the fault planes intersection (highest positive Coulomb stress transfer) and then propagating towards SW, in the region where the slip is promoted.

Secondly, we look at how the two sub-events affect the stress in the surrounding area (Fig. 7b). Specifically, along potential fault planes orientated optimally for thrusting. We aim to understand why there is a lack of aftershocks around the first subevent (Mw 7.1) with a similar thrust mechanism and also assess how Coulomb stress changes due to the doublet along neighbouring structures, potentially hosting future large thrust earthquakes. We find that after the doublet, the surrounding area is not stressed in a way that promotes thrust faulting to the north and south of the first events. This is true even further afield, where the compressional belt to the North, which is very large and potentially tsunamigenic, has a negative value of Coulomb stress change, and the smaller compressional segment to the NW affected by the November 10, 2014 thrust earthquake, which experiences a weak positive Coulomb stress change.

5. Discussion

The study region is quite remote and we lack a proper seismic network, with only one seismic station located at less than 1000 km distance and the majority of stations at thousands kilometers distance. These conditions pose high challenges to the seismological analysis, as regional data are ecsatoo sparse and seismic data at teleseismic distances has a good quality only for the largest events. We tackled these challenges by combining the results of earthquake source analysis, which provide robust results for the largest events only, with a careful assessment and modelling of weaker signals recorded at the few, available close stations (see also Cesca et al., 2020). Such relative earthquake characterization strategy, as well as the specific techniques used in this work, may be helpful for future studies dedicated to remote regions.

Our seismological analysis allows us to reconstruct the evolution of the 2014 JFMP doublet and its seismic sequence, as illustrated in Fig. 8. The first phase (phase 1 in Fig. 8) of the sequence is characterized by the complex rupture of the October 2014 seismic doublet. The rupture started within the JFMP along an EW structure, an already mapped compressional ridge (Larson et al., 1992), and propagated bilaterally East and Westward. Based on the analysis of apparent durations, we suggest the Northward dipping plane as the rupture plane; this is also supported by the asymmetric slope of the ridge seen in the bathymetry, which shows a slightly more gentle slope dipping to the North, and a steeper one to the South (Fig. S8). The second subevent occurred after ~18 min, favoured by Coulomb stress changes imparted by the first subevent along a NE-SW oriented plane, with a strike-slip focal mechanism. The rupture along this second plane, or alternatively along a curved fault bridging the areas of the two events, most likely nucleated at the fault plane intersection and propagated unilaterally towards the SW, in the region which experienced a positive Coulomb stress perturbation after subevent 1. A number of aftershocks were observed in mid October (phase 2) at the sides of the rupture area of subevent 2; most of them are located to the SW, possibly as a consequence of the SW rupture propagation of subevent 2. In phase 3 seismicity slowly decayed and migrated Northward, activating strike-slip structures of different orientation (approximately NNW-SSE) and reaching the vicinity of a second compressional ridge (Larson et al., 1992). Phase 4 (November 2014) is again characterized by a doublet, now starting with a strike-slip mechanism and then continuing into an ~EW thrust earthquake. The spatiotemporal evolution of the sequence highlights the complex rupture interaction and interplay between thrust and strike-slip earthquakes; the two observed doublets display a reverse earthquakes interaction: a first thrust triggered a strike slip event in the October 2014 doublet, while the reverse process (i.e. strike slip-thrust interaction) is observed for the later, November 2014 doublet. We performed a stress inversion within the Northern region of the JFMP based on both the moment tensors of our study and references from other catalogs (i.e. as in Fig. 4). We use an in-house developed inversion, minimizing the radiated seismic energy (Cesca et al., 2016). We constrained the rupture plane orientations only for the first doublet and the early strike-slip aftershocks, which are aligned along a NE-SW pattern compatible with one of the fault planes, and we considered both possible planes for the remaining earthquakes. Our results indicate a predominant compressional regime, with σ_1 oriented NNE-SSW. We found that σ_2 and σ_3 have similar values, so that minor stress perturbations can favour either thrust or strike-slip faulting, explaining the observed cohexistence of different rupture types and occurrence of mixed doublets. Such perturbations

Table 2
Summary of finite source parameters estimated for the earthquake doublet based on the earthquake source parameters (Table 1), shear wave velocity and density from the used velocity model and rupture length and width based on the new empirical laws by Thingbaijam et al. (2017).

Date	Time	Depth [km]	Mw	M_0 [Nm]	Length [km]	Width [km]	Area [km^2]	μ [GPa]	Slip [m]
9.10.2014	02:14:42	5.6	7.06	4.32×10^{19}	43.8	25,2	1103.7	45.7	0.86
9.10.2014	02:32:18	12.3	6.69	1.21×10^{19}	41.0	15.9	651.9	72.6	0.26

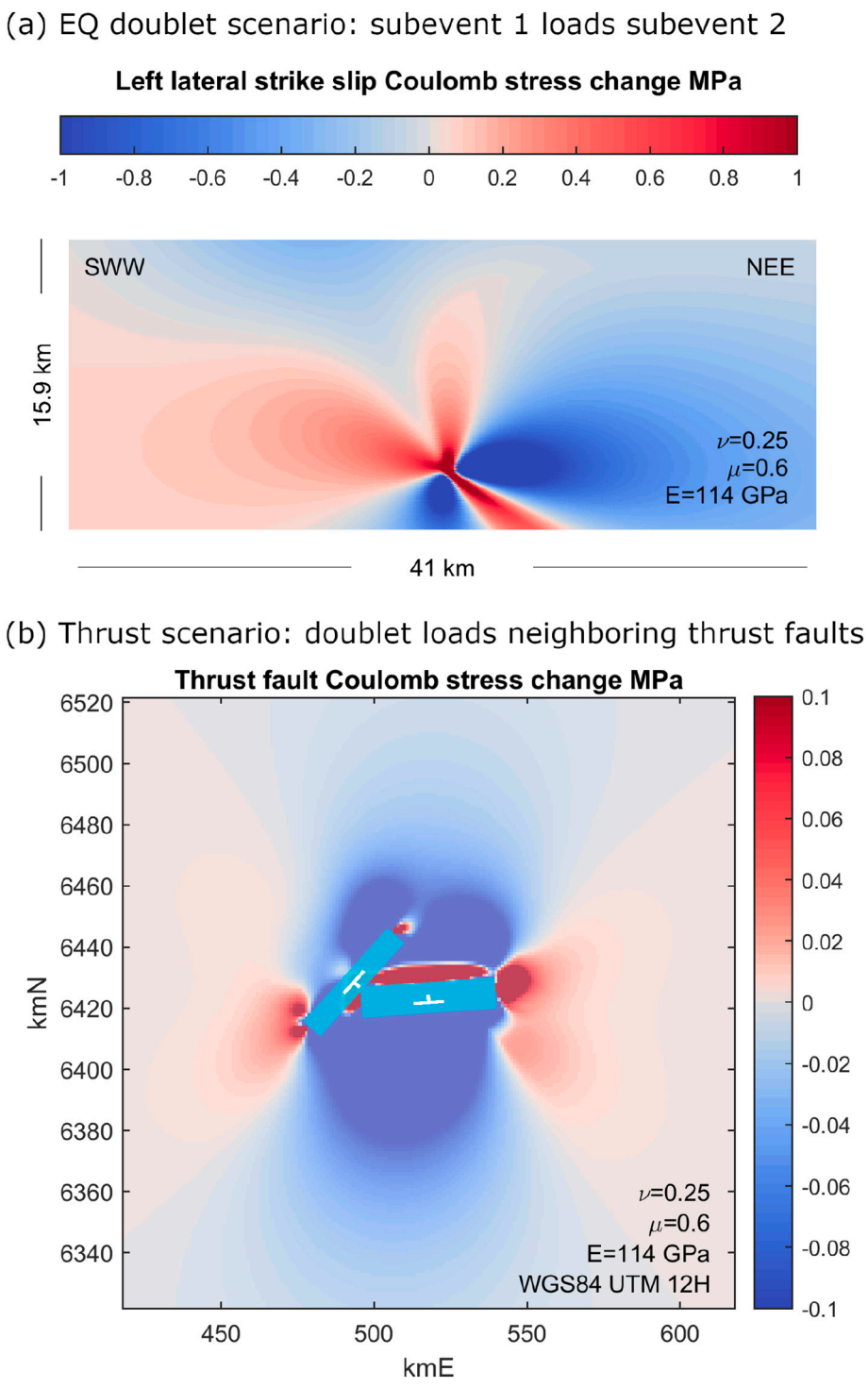

Fig. 7. Result of Coulomb stress changes for two scenarios. (a) Earthquake doublet scenario, with fault plane of subevent 2 loaded by the inverted parameters from subevent 1. Left lateral strike slip Coulomb stress change is calculated on the fault plane of subevent 2. The change in this value halfway corresponds to the junction between the two fault planes. Left-lateral slip is promoted across a large part of the fault plane. (b) Loading on neighbouring thrust faults scenario (the spatial extent of the study region is shown in Fig. 8). Coulomb stress change at a depth of 10 km for potential EW thrust fault planes dipping towards the north at 30 degrees (i.e. mechanism of doublet subevent 1). Stresses are from the earthquake doublet, whose fault planes shown as blue rectangles with white ticks showing their dip direction. The potential for faults of this orientation to slip is reduced in the surrounding area. Both panels report Poisson's ratio (ν), coefficient of friction (μ) and Young's modulus (E). Values of the colour bars are given in MPa. (For interpretation of the references to colour in this figure legend, the reader is referred to the web version of this article.)

could arise from strength anisotropy in the oceanic crust. The latter exhibits a distinct spreading fabric with a preferred N-S to NE-SW orientation in the region affected by the seismic doublets as seen in high resolution bathymetry data (Ryan et al., 2009).

The 2014 JFMP doublet and its following sequence are peculiar due to several aspects: first of all they present outstanding magnitudes, with unprecedented recording in the region. The Mw 7.1 subevent 1 is the largest earthquake ever recorded at the JFMP and its thrust mechanism differs from the majority of the earthquakes in the region, which typically display strike-slip or normal faulting (Fig. 1). While the Northern boundary of the JFMP is considered to undergo compression, thrust mechanisms have been rarely reported there and never with large magnitudes. This observation suggests that regional compressional stresses are in large part accommodated aseismically, e.g. by creeping. Aseismic processes could explain the lack of thrust aftershocks in the 2014 sequence. However, the occurrence of two large shallow thrust fault earthquakes (Mw 7.1 in the October 2014 doublet and Mw 6.1 in the November 2014 doublet) demonstrates that the region can occasionally host strong, impulsive, tsunamigenic earthquakes.

Other aspects of the thrust seismicity at the JFMP are also unusual. First of all, thrust earthquakes at JFMP show an extremely low aftershock productivity on the same fault: we could not detect any single

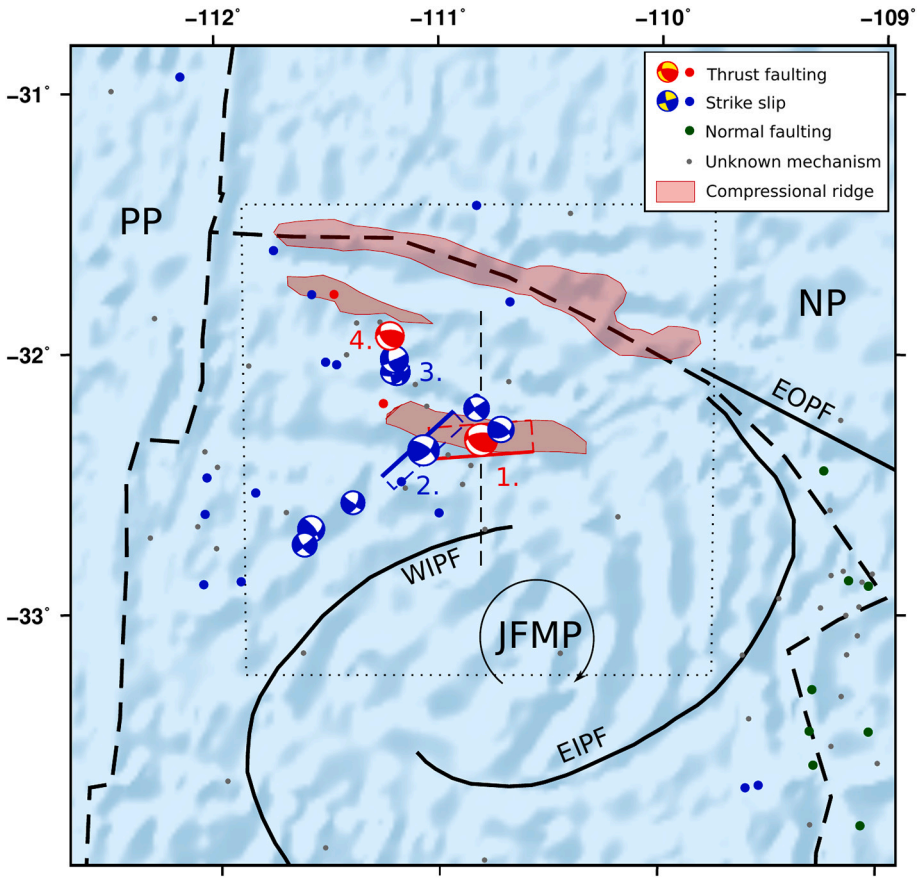

Fig. 8. Resolved evolution of the seismic sequence. Phase 1 includes the bilateral rupture (dashed red rectangle, the top edge of the fault is shown as think solid as line) of the thrust subevent 1 at one compressional ridge (1a), triggering the SW unilateral rupture (dashed blue rectangle, top fault edge as think solid line) of the strike-slip subevent 2 (1b). The following seismic sequence (phase 2) in October, is characterized by abundant strike-slip mechanisms at the edges of subevent 2. Phase 3, in October–November, is marked by the activation of strike-slip activity NW of the first subevent. Phase 4, in November, shows the second doublet, starting with a strike-slip mechanism (4a) and continuing with the activation of thrust faulting in a second compressional ridge 4b). The figure reports the West ridge Inner Pseudofault (WIPF), East ridge Inner Pseudofault (EIPF), East ridge outer Pseudofault (EOPF) and compressional ridges, as mapped by Larson et al. (1992), major plate boundaries (after Bird (2003) and the current rotation direction (curved arrow) of the Juan Fernández Microplate (JFMP). A dotted square indicates the spatial extent of Fig. 7b; the bathymetry along the NS profile (dashed line) is shown in Fig. S8. (For interpretation of the references to colour in this figure legend, the reader is referred to the web version of this article.)

thrust aftershock after the Mw 7.1 thrust earthquake, whereas the substantially weaker Mw 6.7 subevent 2, with a strike-slip mechanism, was followed by several aftershocks with a similar focal mechanism. This can be partially attributed to aseismic processes, as well as a low (if not negative) Coulomb stress loading on neighbouring thrust faults. The two thrust earthquakes also show an unusually short duration: this can be partially explained, at least for the first subevent of the October doublet, by its bilateral rupture propagation able to break a large segment (~45 km) in a relatively short time (10 s).

While most of the previous seismicity at the JFMP displayed typical characteristics of interplate seismicity, with alternating between strike-slip and normal fauling segments along the JFMP boundaries, the 2014 sequence clearly occurred within the JFMP, even accounting for location uncertainties, which are below 10 km for hypocenters and ~25 km for centroids. We question whether the doublet activated the West Internal pseudofault (WIPF). The geometry of the activated fault segments resembles the proposed pseudofault lineament, but earthquake locations appear shifted to the North. However, the pseudofaults about the West Ridge are less clear than those on the East Ridge and the trace of the West Ridge inner pseudofault, in particular, is poorly resolved and obscured by volcanism (Larson et al., 1992). In these conditions, we suggest this is the activation of the inner pseudofault, but cannot verify this. Location and focal mechanisms of thrust earthquakes are also well compatible with the location and orientation of compressional ridges, and the sequence evolution suggests the consequent activation of different ridges migrating Northward from October to November: to date, the largest and Northernmost ridge, in the vicinity of the PP-NP-JFMP triple junction remains unbroken.

Is there any tsunami hazard in the South Pacific, far from any subduction zone? The tsunami reported after the 2014 earthquake was relatively weak, with the largest run up height of ~50 cm at Easter Island at ~600 km distance. This tsunami is most likely to be attributed to the first subevent, which has a larger tsunamigenic potential due to both its larger magnitude, shallower centroid, impulsive source and thrust mechanism. The tsunami hazard should take into account the potential failure of other segments under compression. A large compressional ridge has been mapped at the Northern boundary of the JFMP (Larson et al., 1992), with a lateral extent of ~200 km, thus more than 4 times longer than the rupture of the October 2014 thrust, and a potential to host an earthquake with magnitude Mw ~8.1 (based on the empirical relation by Thingbaijam et al., 2017). It is worth noting that, according to Coulomb stress modelling (Fig. 7b), the 2014 doublet has inhibited or delayed a thrust failure of the Northern compressional belt. Assuming the same shear modulus and the same seismogenic thickness for thrust earthquakes in the region (i.e. same width for different thrust events), such potential earthquake would have a ~ 4 times larger area than the October 2014 one and ~ 35 times larger moment release. Using the following equation to relate scalar moment (M_0), rupture area (A), average slip (λ) and shear modulus (μ):

$$\lambda_2 = \frac{M_{0,2}}{A_2\mu} = \frac{M_{0,1}\left(M_{0,2}/M_{0,1}\right)}{A_1(L_2/L_1)\mu} = \lambda_1\frac{\left(M_{0,2}/M_{0,1}\right)}{(L_2/L_1)} \quad (1)$$

we estimate an average slip ~8 times larger than for the 2014 thrust (in eq. (1), subindices 1 and 2 refer to the reference Mw 7.1 subevent 1 and the potential Mw 8.1 earthquakes, respectively). Since we investigate the scenario of a thrust earthquakes with a similar mechanism and at a similar location and depth, the potential tsunami run up height would be at least ~8 times larger than for the 2014 event, thus reaching ~4 m at Easter Island, Chile, and almost 1 m at Galapagos, Ecuador, and at San Felix and Bahia Mansa, Chile, if the large unbroken thrust ruptures.

6. Conclusions

The 2014 seismic sequence struck at the JFMP with an unprecedented magnitude for the region, peaking in a Mw 7.1 earthquake on October 9, 2014 with a thrust focal mechanism, which is also unusual for the region. Besides the remoteness of this region, we combined different waveform based seismological techniques to analyse this seismic sequence. Rather than appearing as a simple mainshock-aftershock sequence, seismicity has been characterized by a complex sequence, including two doublets with an uneven mechanism, the Mw 7.1–6.7 thrust and strike-slip mechanism in October 2014 and a weaker, later Mw 5.9–6.1 strike-slip and thrust mechanism in November 2014. Apart from having a large magnitude, the seismic sequence was anomalous due to its alternation of strike-slip and thrust mechanisms, that indicates the activation of different faults or fault segments. Using a variety of seismological techniques to tackle the lack of local observations, we were able to reconstruct the chronology and geometry of this complex seismic sequence. This started with the large doublet, rupturing EW and NE-SW fault segments in the vicinity of a known compressional ridge, or alternatively a single curved pseudofault (WIPF). The following seismicity was first marked by strike-slip aftershocks of the first doublet and, later, by a Northward migration towards a second compressional ridge, where the second doublet occurred. We identified specific features of the thrust seismicity, namely low aftershock productivity, short duration and impulsive sources. Together with the overall low rate thrust seismicity, this suggests that the compressional stresses at the North of the JFMP are partially accommodated aseismically, with the occasional occurrence of thrust earthquakes. Thus, the sequence demonstrated that the region has a potential to host large, tsunamigenic earthquakes in the future. A worst case scenario, assuming the rupture along a 200 km long compressional ridge at the Northern boundary of the JFMP, could produce a ~ 4 m height tsunami at Easter Island. Coulomb stress changes imparted by the 2014 doublet have currently slightly reduced the failure potential along this ridge. The unexpected characteristics of the 2014 doublet and its seismic sequence indicate that we still poorly know the behaviour of the JFMP and its seismicity, and that a new local study and submarine seismic deployments would be desirable. Our study shines some more light on the occurrence of such complex seismic sequence in the region. As the roller-bearing microplate faults and step-over systems are often observed at oceanic plate boundaries, the occurrence of the JFMP seismic sequence provides a model for the generation of tsunamis at mid oceanic ridges.

Data availability

Seismic data used in this study have been accessed using IRIS, Geofon and Orfeus web service portals. Seismic data belongs to the following networks: II (Scripps Institution Of Oceanography (1986), IU (Albuquerque Seismological Laboratory (ASL)/USGS (1988), G (Institut De Physique Du Globe De Paris (IPGP), and Ecole Et Observatoire Des Sciences De La Terre De Strasbourg (EOST), 1982), AI (Istituto Nazionale Di Oceanografia E Di Geofisica Sperimentale, 1992), C (Universidad de Chile, Dept de Geofisica, DGF UChile Chile), C1 (Universidad De Chile, 2013)., CX (GFZ German Research Centre For Geosciences and Institut Des Sciences De L'Univers-Centre National De La Recherche CNRS-INSU, 2006), GT (Albuquerque Seismological Laboratory (ASL)/USGS, 1993) and IQ (Cesca et al., 2009). We made use of the ISC Bulletin (International Seismological Centre, 2020), Global CMT catalog (Dziewonski et al., 1981; Ekström et al., 2012) and USGS seismic catalog (https://earthquake.usgs.gov/, last accessed 1.7.2020).

CRediT authorship contribution statement

Simone Cesca: Conceptualization, Methodology, Writing - original draft, Visualization. **Carla Valenzuela Malerán:** Data curation, Methodology, Visualization. **José Ángel López-Comino:** Methodology, Visualization. **Timothy Davis:** Methodology, Visualization, Writing - review & editing. **Carlos Tassara:** Data curation. **Onno Oncken:** Writing - review & editing. **Torsten Dahm:** Methodology, Writing - review & editing.

Declaration of Competing Interest

None.

Acknowledgements

We are thankful to the editor, Dr. K. Wang, to Prof. Dr. J. Zahradník and to an anonymous reviewer for careful reviews and useful suggestions. We used pyrocko (Heimann et al., 2017) for processing and for the generation of some figures. C.V.M. appreciates the scholarship granted to her by the National Commission for Scientific and Technological Research (CONICYT – Becas Chile), N° 72180072. J.A.L.C. has received funding from the European Union's Horizon 2020 Research and Innovation Programme under the Marie Skłodowska-Curie Grant agreement N° 754446 and UGR Research and Knowledge Transfer Found – Athenea3i; and by the Deutsche Forschungsgemeinschaft (DFG, German Research Foundation) – Projektnummer (407141557). T. Davis is funded by the DFG-ICDP grant N. RI 2782/3-1.

Appendix A. Supplementary data

Supplementary data to this article can be found online at https://doi.org/10.1016/j.tecto.2021.228720.

References

Albuquerque Seismological Laboratory (ASL)/USGS, 1988. Global Seismograph Network (GSN - IRIS/USGS). International Federation of Digital Seismograph Networks. https://doi.org/10.7914/SN/IU.

Albuquerque Seismological Laboratory (ASL)/USGS, 1993. Global Telemetered Seismograph Network (USAF/USGS). International Federation of Digital Seismograph Networks. https://doi.org/10.7914/SN/GT.

Anderson, R.N., Forsyth, D.W., Molnar, P., Mammerickx, J., 1974. Fault plane solutions and earthquakes on the Nazca plate boundaries and the Easter Plate. Earth Planet. Sci. Lett. 24, 188–202.

Anderson-Fontana, S., Engeln, J.F., Lundgren, P., Larson, R.L., Stein, S., 1986. Tectonics and evolution of the Juan Fernandez microplate at the Pacific-Nazca-Antarctic triple junction. J. Geophys. Res. 91, 2005–2018.

Astiz, L., Kanamori, H., 1984. An earthquake doublet in Ometepec, Guerrero, Mexico. Phys. Earth Planet. Int. 34, 24–45.

Barazangi, M., Dorman, J., 1969. World seismicity maps compiled from ESSA Coast and Geodetic Survey epicentral data. Bull. Seism. Soc. Am. 59, 369.

Bird, P., 2003. An updated digital model of plate boundaries. Geochem. Geophys. Geosyst. https://doi.org/10.1029/2001GC000252.

Bird, R.T., Nar, D.F., Larson, R.L., Searle, R.C., Scotese, C.R., 1998. Plate tectonic reconstructions of the Juan Fernandez microplate: transformation from internal shear to rigid rotation. J. Geophys. Res. 103 (B4), 7049.

Cesca, S., Sobiesiak, M., Tassara, C., Olcay, M., Günther, E., Mikulla, S., Dahm, T., 2009. The Iquique Local Network and PicArray. GFZ Data Services. Other/Seismic Network. https://doi.org/10.14470/VD070092.

Cesca, S., Heimann, S., Dahm, T., 2011. Rapid directivity detection by azimuthal amplitude spectra inversion. J. Seismol. 15 (1), 147–167. https://doi.org/10.1007/s10950-010-9217-4.

Cesca, S., Grigoli, F., Heimann, S., Dahm, T., Kriegerowski, M., Sobiesiak, M., Tassara, C., Olcay, M., 2016. The Mw 8.1 2014 Iquique, Chile, seismic sequence: a tale of foreshocks and aftershocks. Geophys. J. Int. 204 (3), 1766–1780. https://doi.org/10.1093/gji/ggv544.

Cesca, S., Letort, J., Razafindrakoto, H.N.T., Heimann, S., Rivalta, E., Isken, M.P., Nikkhoo, M., Passarelli, L., Petersen, G., Cotton, F., Dahm, T., 2020. Drainage of a deep magma reservoir near Mayotte inferred from seismicity and deformation. Nat. Geosci. 13 (1), 87–93. https://doi.org/10.1038/s41561-019-0505-5.

Craig, H., Kim, K.R., Francheteau, J., 1983. Active ridge crest mapping on the Juan Fernandez microplate: The use of Sea Beam-controlled hydrothermal plume surveys. Eos Trans, AGU 64, 45.

Danré, P., Yin, J., Lipovsky, B.P., Denolle, M.A., 2019. Earthquakes within earthquakes: patterns in rupture complexity. Geophys. Res. Lett. 46, 7352–7360. https://doi.org/10.1029/2019GL083093.

Dziewonski, A.M., Chou, T.-A., Woodhouse, J.H., 1981. Determination of earthquake source parameters from waveform data for studies of global and regional seismicity. J. Geophys. Res. 86, 2825–2852. https://doi.org/10.1029/JB086iB04p02825.

Ekström, G., Nettles, M., Dziewonski, A.M., 2012. The global CMT project 2004-2010: centroid-moment tensors for 13,017 earthquakes. Phys. Earth Planet. Int. 200-201, 1–9. https://doi.org/10.1016/j.pepi.2012.04.002.

Forsyth, D.W., 1972. Mechanisms of earthquakes and plate motions in the east Pacific. Earth Planet. Sci. Lett. 17 (1), 189–193. https://doi.org/10.1016/0012-821X(72)90275-0.

Francheteau, J., Yelles-Chaouche, A., Craig, H., 1987. The Juan Fernandez microplate north of the Pacific-Nazca-Antarctic plate junction at 35° S. Earth Planet. Sci. Lett. 86 (2–4), 253–268.

GFZ German Research Centre For Geosciences and Institut Des Sciences De L''Univers-Centre National De La Recherche CNRS-INSU, 2006. IPOC Seismic Network. Integrated Plate boundary Observatory Chile - IPOC. https://doi.org/10.14470/PK615318.

Ghods, A., Shabanian, E., Bergman, E., Faridi, M., Donner, S., Mortezanejad, G., Aziz-Zanjani, A., 2015. The Varzaghan–Ahar, Iran, Earthquake Doublet (M_w 6.4, 6.2): implications for the geodynamics of northwest Iran. Geophys. J. Int. 203 (1), 522–540. https://doi.org/10.1093/gji/ggv306.

Haskell, N.A., 1964. Total energy and energy spectral density of elastic wave radiation from propagating faults. Bull. Seism. Soc. Am. 54, 1811–1841.

Heimann, S., Kriegerowski, M., Isken, M., Cesca, S., Daout, S., Grigoli, F., Juretzek, C., Megies, T., Nooshiri, N., Steinberg, A., Sudhaus, H., Vasyura-Bathke, H., Willey, T., Dahm, T., 2017. Pyrocko - An Open-source Seismology Toolbox and Library, vol. 0.3. GFZ Data Services. https://doi.org/10.5880/GFZ.2.1.2017.001.

Heimann, S., Isken, M., Kühn, D., Sudhaus, H., Steinberg, A., Vasyura-Bathke, H., Daout, S., Cesca, S., Dahm, T., 2018. Grond - A Probabilistic Earthquake Source Inversion Framework, vol. 1.0. GFZ Data Services. https://doi.org/10.5880/GFZ.2.1.2018.003.

Herron, E., 1972. Two small crustal plates in the South Pacific near Easter Island. Nat. Phys. Sci. 240, 35–37. https://doi.org/10.1038/physci240035a0.

Hey, R.N., 1977. A new class of pseudofaults and their bearing on plate tectonics: a propagating rift model. Earth Planet. Sci. Lett. 37, 321–325.

Hey, R.N., Johnson, P.D., Martinez, F., Korenaga, J., Somers, M.L., Huggett, Q.J., LeBas, T.P., Rusby, R.I., Naars, D.F., 1995. Plate boundary reorganization at a large-offset, rapidly propagating rift. Nature 378, 167–170.

Institut De Physique Du Globe De Paris (IPGP), Ecole Et Observatoire Des Sciences De La Terre De Strasbourg (EOST), 1982. GEOSCOPE, French Global Network of Broad Band Seismic Stations. Institut de Physique du Globe de Paris (IPGP). https://doi.org/10.18715/GEOSCOPE.G.

International Seismological Centre, 2020. On-line Bulletin. https://doi.org/10.31905/D808B830.

Istituto Nazionale Di Oceanografia E Di Geofisica Sperimentale, 1992. Antarctic Seismographic Argentinean Italian Network (ASAIN). International Federation of Digital Seismograph Networks. https://doi.org/10.7914/SN/AI.

Kagan, Y.Y., Jackson, D.D., 1999. Worldwide doublets of large shallow earthquakes. Bull. Seismol. Soc. Am. 89 (5), 1147–1155.

King, G.C., Stein, R.S., Lin, J., 1994. Static stress changes and the triggering of earthquakes. Bull. Seismol. Soc. Am. 84 (3), 935–953.

Larson, R.L., Searle, R.C., Kleinrock, M.C., Schouten, H., Bird, R.T., Naar, D.F., Rusby, R. I., Hooft, E.E., Lasthiotakis, H., 1992. Roller-bearing tectonic evolution of the Juan Fernandez microplate. Nature 356.

Lay, T., Kanamori, H., 1980. Earthquake doublets in the Solomon Islands. Phys. Earth Planet. Int. 21 (4), 283–304. https://doi.org/10.1016/0031-9201(80)90134-X.

Lay, T., Duputel, Z., Ye, L., Kanamori, H., 2013. Interactions between near-trench intraplate thrust and normal faulting. Phys. Earth Planet. Int. 220, 73–78. https://doi.org/10.1016/j.pepi.2013.04.009.

Liu, J., Zahradník, J., 2020. The 2019 M_W 5.7 Changning earthquake, Sichuan Basin, China: a shallow doublet with different faulting styles. Geophys. Res. Lett. 47. https://doi.org/10.1029/2019GL085408.

López-Comino, J.A., Mancilla, F., Morales, J., Stich, S., 2012. Rupture directivity of the 2011, Mw 5.2 Lorca earthquake (Spain). Geophys. Res. Lett. 39, 3. https://doi.org/10.1029/2011GL050498.

López-Comino, J.A., Stich, D., Morales, J., Ferreira, A.M.G., 2016. Resolution of rupture directivity in weak events: 1-D versus 2-D source parameterizations for the 2011, Mw 4.6 and 5.2 Lorca earthquakes, Spain. J. Geophys. Res. 121, 6608–6626. https://doi.org/10.1002/2016JB013227.

Martinez, F., Hey, R.N., Johnson, P.D., 1997. The East ridge system 28.5–32#S East Pacific rise: implications for overlapping spreading center development. Earth Planet Sci. Lett. 151, 13–31.

Naar, D.F., Bird, R.T., Rusby, R.I., 1991. A tale of two microplates: comparison of Juan Fernandez and Easter. Eos (Transactions, American Geophysical Union) 72, 509.

Niazpour, B., Shomali, Z.H., Cesca, S., 2020. Source study of 2017 Hojedk triplet earthquake sequence, southeast Iran. J. Seismol. https://doi.org/10.1007/s10950-020-09934-3.

Nikkhoo, M., Walter, T.R., 2015. Triangular dislocation: an analytical, artefact-free solution. Geophys. J. Int. 201 (2), 1119–1141.

Ryan, W.B.F., Carbotte, S.M., Coplan, J.O., O'Hara, S., Melkonian, A., Arko, R., Weissel, R.A., Ferrini, V., Goodwillie, A., Nitsche, F., Bonczkowski, J., Zemsky, R., 2009. Global multi-resolution topography synthesis. Geochem. Geophys. Geosyst. 10, Q03014 https://doi.org/10.1029/2008GC002332.

Schouten, H., Gallo, D.G., Klitgord, K.D., 1988. Microplate kinematics of the second order. EOS Trans. Am. Geophys. Union 69, 488.

Scripps Institution Of Oceanography, 1986. IRIS/IDA Seismic Network. International Federation of Digital Seismograph Networks. https://doi.org/10.7914/SN/II.

Searle, R.C., Bird, R.T., Rusby, R.I., Naar, D.F., 1993. Development of two oceanic microplates: Easter and Juan Fernandez microplates, East Pacific Rise. J. Geol. Soc. Lond. 150, 965–976.

Smith, G.P., Ekström, G., 1996. Interpretation of earthquake epicenter and CMT centroid locations, in terms of rupture length and direction. Phys. Earth Planet. Int. 102, 123–132.

Sykes, L.R., 1967. Mechanism of earthquakes and nature of faulting on the mid-oceanic ridges. J. Geophys. Res. 72, 2131.

Thingbaijam, K.K.S., Mai, P., Goda, K., 2017. New empirical earthquake source-scaling laws. Bull. Seismol. Soc. Am. 107, 2225–2246. https://doi.org/10.1785/0120170017.

Tilmann, F., Zhang, Y., Moreno, M., Saul, J., Eckelmann, F., Palo, M., Deng, Z., Babeyko, A.Y., Chen, K., Baez, J.C., Schurr, B., Wang, R., Dahm, T., 2016. The 2015 Illapel earthquake, central Chile: a type case for a characteristic earthquake? Geophys. Res. Lett. 43 (2), 574–583. https://doi.org/10.1002/2015GL066963.

Universidad De Chile, 2013. Red Sismologica Nacional. International Federation of Digital Seismograph Networks. https://doi.org/10.7914/SN/C1.

Vallée, M., Douet, V., 2016. A new database of Source Time Functions (STFs) extracted from te SCARDEV method. Phys. Earth Planet. Int. 257, 149–157.

Yelles-Chaouche, A., Francheteau, J., Patriat, Ph., 1987. Evolution of the Juan Fernandez microplate during the last three million years. Earth Planet. Sci. Lett. 86 (2–4), 269–286.

Zahradnik, J., Gallovic, F., Sokos, E., Serpetsidaki, A., Tselentis, G.A., 2008. Quick fault-plane identification by a geometrical method: application to the Mw6.2 Leonidio earthquake, January 6, 2008, Greece. Seismol. Res. Lett. 79, 653–662.

Zahradník, J., Čížková, H., Bina, C., Sokos, E., Janský, J., Tavera, H., Carvalho, J., 2017. A recent deep earthquake doublet in light of long-term evolution of Nazca subduction. Sci. Rep. 7, 45153. https://doi.org/10.1038/srep45153.